Research Article

Photoacoustic imaging driven by an interstitial irradiation source

Trevor Mitcham [a,c], Katherine Dextraze [a,c], Houra Taghavi [a], Marites Melancon [b,c], Richard Bouchard [a,c]

[a] Department of Imaging Physics, University of Texas MD Anderson Cancer Center, Houston, TX 77030, USA
[b] Department of Interventional Radiology, University of Texas MD Anderson Cancer Center, Houston, TX 77030, USA
[c] Graduate School of Biomedical Sciences, University of Texas at Houston, Houston, TX 77030, USA

ARTICLE INFO

ABSTRACT

Photoacoustic (PA) imaging has shown tremendous promise in providing valuable diagnostic and therapy-monitoring information in select clinical procedures. Many of these pursued applications, however, have been relatively superficial due to difficulties with delivering light deep into tissue. To address this limitation, this work investigates generating a PA image using an interstitial irradiation source with a clinical ultrasound (US) system, which was shown to yield improved PA signal quality at distances beyond 13 mm and to provide improved spectral fidelity. Additionally, interstitially driven multi-wavelength PA imaging was able to provide accurate spectra of gold nanoshells and deoxyhemoglobin in excised prostate and liver tissue, respectively, and allowed for clear visualization of a wire at 7 cm in excised liver. This work demonstrates the potential of using a local irradiation source to extend the depth capabilities of future PA imaging techniques for minimally invasive interventional radiology procedures.

1. Introduction

In the past twenty years, image guidance has been utilized increasingly to improve the precision and efficacy of diagnostic and therapeutic procedures [1]. Typically, image guidance is provided by ultrasound (US), X-ray computed tomography, fluoroscopy, or magnetic resonance imaging. Photoacoustic (PA) imaging is a promising technique that is non-ionizing, low-cost, and offers high-contrast imaging of both the surgical tools and photoabsorbers that are often encountered in diagnostic and therapeutic techniques. To provide accurate guidance, PA images can be co-registered with US imaging to generate a photoacoustic-ultrasonic (PAUS) image that contains clear anatomical information and provides high-contrast visualization of important photoabsorbers, such as hemoglobin or targeted nanoparticles [2]. To date, however, the application of PAUS imaging has typically been limited to superficial anatomical sites due to the relatively shallow penetration depth of the external irradiation source.

PA imaging requires a narrow-pulse-width laser irradiation source, photoabsorbers to generate PA-induced pressure waves, and an US transducer for signal detection. The light provided by the pulsed irradiation source is absorbed by photoabsorbers and immediately converted to heat. This thermal transient leads to rapid local expansion, creating pressure waves that can be detected with high spatiotemporal resolution by an US transducer. The resulting pressure waves are dependent on local fluence, optical absorption, and thermally dependent material properties [3]. The initial local pressure (p_0) generated by the PA effect can be described as

$$p_o = \frac{\beta c^2}{C_p}\mu_a F = \Gamma A, \tag{1}$$

where $\beta [\frac{1}{K}]$ is the thermal coefficient of volume expansion, $c [\frac{m}{s}]$ is the speed of sound through tissue, $C_p [\frac{J}{K \cdot kg}]$ is the heat capacity at constant pressure, $\mu_a [\frac{1}{cm}]$ is the optical absorption coefficient, $F [\frac{J}{cm^2}]$ is the local laser fluence, Γ is the Grüneisen coefficient, and $A [\frac{J}{cm^3}]$ is the local deposition energy.

As laser light travels through a medium (e.g., tissue), fluence is lost due to optical scattering and absorption by tissue components like blood and adipose tissue. This fluence loss is the primary cause of the limited depth penetration that has previously hindered the clinical application of PA imaging. Compensating for fluence loss is a nuanced problem. The laser fluence applied to skin in clinical applications is regulated by the American National Standards Institute (ANSI), which recommends that clinical skin exposure to low near-infrared (NIR) light not exceed specific fluence levels

E-mail address: rrbouchard@mdanderson.org.

ranging from 20 $\frac{mJ}{cm^2}$ at 700 nm, to 50 $\frac{mJ}{cm^2}$ at 900 nm, to 100 $\frac{mJ}{cm^2}$ at 1050 nm [4,5]. Therefore, depth penetration cannot be improved by simply increasing surface fluence. Previous work has explored using a 1064-nm wavelength laser for PA imaging applications. At this wavelength, tissue scattering and absorption is decreased compared to lower NIR wavelengths, while the exposure limitations through skin rise linearly to 100 $\frac{mJ}{cm^2}$, providing a situation in which more laser light can be delivered to target photoabsorbers [4–6]. The reduction in tissue scattering and absorption at 1064 nm also results in reduced background signal in PA images, which improves the contrast of the images compared to imaging at lower wavelengths in the NIR range [7]. However, the depth penetration with 1064-nm irradiation can still be quite limited for clinical applications, and such an implementation can restrict opportunities for multi-wavelength imaging. One final method to improve imaging depth is to fundamentally change the absorption properties of the target being imaged, a technique that has been demonstrated for metallic objects [8].

To circumvent the depth penetration limitation of NIR irradiation, endoscopic, intravascular and transrectal PA imaging techniques have been developed for targeting deeper tissues [9–14]. Although these techniques have been effective for imaging particular structures, such as the prostate, colon, or vascular wall, they have not been applied more generally to deep-tissue imaging. Furthermore, the smaller US transducers that are used to accommodate PA endoscopic or intravascular imaging have lower sensitivity and a reduced receive-aperture extent (compared to larger, more conventional US arrays), resulting in reduced image quality [15]. Therefore, in order to deliver light to deep tissues while maintaining image quality, an interstitial optical source could be introduced to provide local irradiation of the target, while a conventional diagnostic US array could be used for external acoustic detection and PA image formation.

This work investigated the use of a single interstitial optical fiber co-registered with an external US transducer to provide PA images for specific interventional radiology (IR) procedures (e.g., laser ablation or biopsy guidance). Optical fibers were modified to serve as a local, interstitial irradiation source. To demonstrate initial feasibility of the interstitial PA imaging system, wire targets, gold nanoshells (AuNSs), and deoxyhemoglobin were imaged in tissue-mimicking phantoms and in ex-vivo tissue.

2. Materials and methods

2.1. General setup and fiber processing

The imaging setup consisted of a pulsed laser source that triggered the receive acquisition of a clinical US system. A Quanta-Ray® PRO pulsed Nd:YAG laser coupled into a tunable GWU versaScan optical parametric oscillator (OPO; Newport Corp., Irvine, CA) was used to provide pulsed NIR irradiation. After exiting the OPO, the beam was sent through a neutral-density filter to a plano-convex focusing lens (Thorlabs Inc., Newton, NJ) that adjusted the spot size to allow for better coupling into optical fibers with a 1000-μm diameter. This diameter was chosen because it coincides with the size of needles often used in biopsy procedures, providing more clinically relevant implantation of the fiber into the tested phantoms [16]. After the focusing lens, a custom-built fiber holder was connected to a three-dimensional micrometer-driven platform to allow for precision translation of the fiber coupling stage (MBT616D; Thorlabs Inc., Newton, NJ). From the coupling stage, the fiber was inserted into a phantom and used to generate a PA signal that was detected with a Vantage 128 US system using an L11-4v linear array operating at 6.25 MHz (Verasonics, Inc., Redmond, WA). A schematic of the complete
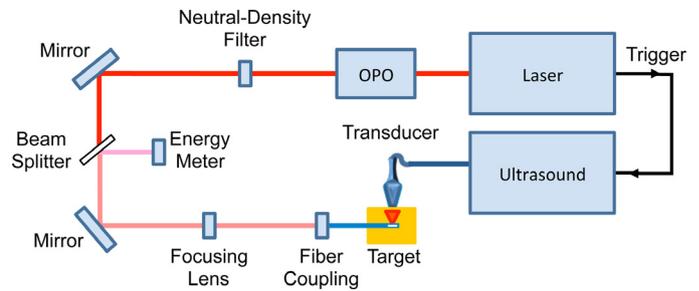

Fig. 1. Schematic of PA imaging system driven by an interstitial irradiation source.

system setup is provided in Fig. 1. Pulse energy readings were taken with a Nova II meter connected to a PE50-DIF-ER-V2 detector with diffuser (Ophir Optronics Solutions Ltd., Jerusalem, Israel) while laser wavelength was calibrated using a Thorlabs CCS175 compact spectrometer (Thorlabs Inc., Newton, NJ). Energy delivery to the fiber was estimated by splitting the primary beam into the energy meter using a glass slide. The energy meter was also placed at the irradiating side of each fiber prior to a study to determine the wavelength-dependent ratio between measured input energy and output energy. This ratio and the estimated input energy values obtained from the beam splitter were utilized to normalize for output fluence differences between wavelengths. Additionally, laser spot size measurements were taken by coupling a continuous wave (CW) laser into the fiber and measuring the projected spot at 5 mm from the fiber tip.

Two different types of 1000-μm-diameter fibers were used in this study. All but one study utilized custom-built, side-fire 1000-μm fibers (Fig. 2.d; Thorlabs Inc., Newton, NJ). In order for optical fibers to transmit light efficiently, both the proximal (i.e., the end coupled to the incoming laser beam) and distal (i.e., the end acting as a local optical source) ends of the fiber must be beveled to appropriate angles and minimized of surface imperfections [12]. Proximal ends were left flat, polished, then qualitatively inspected using a digital microscope (zipScope; Aven Inc., Ann Arbor, MI,) to ensure surface smoothness (Fig. 2.b-c). If any scratches or cloudy areas were present, the polishing sequence was repeated until the surface appeared visually smooth. Upon completion of the proximal fiber tip, the distal tip was sanded using a custom-built, angled sanding apparatus (Fig. 2.a) until the tip was beveled to a critical angle of 35°; it was then polished in a similar fashion to the procedure implemented for the proximal tip. The distal tip was beveled to promote total internal reflection, which allows the fiber to emit light perpendicularly (i.e., side-fire) rather than out the tip (i.e., straight-fire) [12]. As the coupling medium at the end of the fiber determines the critical angle needed, quartz end-caps were added (Sutter Instrument Co., Novato, CA) to ensure that the fiber tip was always air-backed. The spot size 5 mm lateral from the tip was measured to be approximately 0.2 cm^2. Side-fire fibers were implemented in the majority of the studies as they could be readily produced in-house and they tended to provide increased fluence in their limited irradiation volume.

The last study utilized a clinically-approved fiber with a conical distal tip that provided 360° irradiation from a 35° half angle at the distal tip with a spot size of 2.5 cm^2 (i.e., 3.1 cm circumference and 0.8 cm height) at a lateral distance of 5 mm (Fig. 2.e; Pioneer Optics Co., Bloomfield, CT); this fiber is typically used for administration of photodynamic therapy.

All tissue-mimicking phantoms used in this investigation were created using 8% (wt%) gelatin (Sigma-Aldrich Co., St. Louis, MO), 5% Intralipid® (Sigma-Aldrich, St. Louis, MO), 1% silica (US Silica, Frederick, MD), 0.1% formaldehyde (Sigma-Aldrich Corp., St. Louis, MO), and 85.9% deionized (DI) H$_2$O in order to generally mimic the
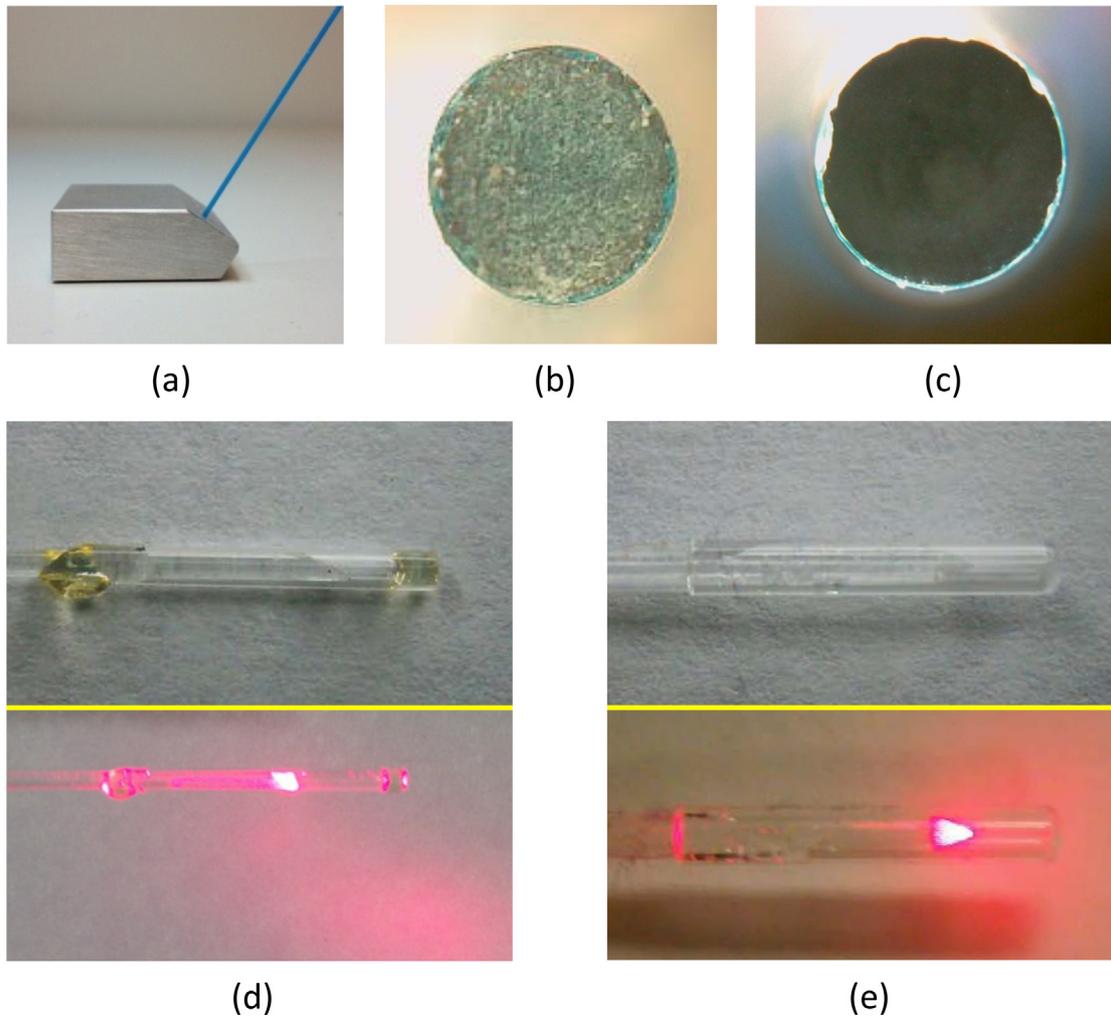
Fig. 2. Optical fiber polishing block, stages of fiber preparation, and completed fiber tips and CW irradiation patterns. (a) Beveled fiber block allows for creation of 35° angle on distal fiber tip for light deflection. (b) Magnified image of proximal fiber tip before sanding or polishing. (c) Magnified fiber tip after polishing with 5-μm polishing film. (d) Magnified capped side-fire fiber tip (top) and CW irradiation pattern (bottom). (e) Magnified capped conical-tip fiber (top) and CW irradiation pattern (bottom).

acoustic and optical properties of tissue [17]. For all studies using interstitial irradiation, the fiber source was placed approximately 5 mm laterally from the imaging target, while PA-induced acoustic signal generation was detected with an external linear US transducer. Pulse-echo US was then used to align the imaging plane with the target of interest. All data presented were normalized for wavelength-dependent differences in surface/fiber fluence. Quantitative analysis of PA data was achieved by selecting a region of interest (ROI) that included only the desired photoabsorber (e.g., titanium wire). In all plots with error bars, the average and standard deviation for each point is presented; the specific sample number for each plot is provided in the figure caption.

2.2. Tissue-mimicking depth phantom

To demonstrate the improvement in depth penetration when using interstitial irradiation, the first study imaged wires at increasing depth within a tissue-mimicking phantom using both interstitial and conventional (i.e., external) laser irradiation. Due to the geometry of the laser setup (Fig. 1), conventional irradiation had to occur from the side while the US probe was placed on top of the phantom. Wire targets were placed in the phantom along a diagonal line with increasing depth. Given this construction, the distance traveled by the photons (d_p) was approximately equal to the acoustic propagation distance (d_a) to the transducer (Fig. 3.a). Wires were included at 7, 20, 37, and 47 mm depths (d_a) with corresponding

lateral offsets (d_p) of 13, 23, 35, and 46 mm. Note that the first wire was displaced more laterally than initially desired to allow for adequate transducer positioning at the edge of the phantom. Using conventional irradiation, 35-40 mJ of energy at 800 nm entered the surface of the phantom (approximately 0.8 cm^2 spot size). In comparison, when using interstitial irradiation, pulse energy was only 6 mJ at 720 nm (i.e., 30 $\frac{mJ}{cm^2}$ at 5 mm) and had a maximum energy of 8 mJ at 900 nm (i.e., 40 $\frac{mJ}{cm^2}$ at 5 mm). Signal-to-noise ratio (SNR) and contrast-to-noise ratio (CNR) were calculated as [18,19]

$$\text{SNR} = \frac{\overline{S_i}}{\sigma_o}, \text{CNR} = \frac{\overline{S_i} - \overline{S_o}}{\sqrt{\sigma_i^2 + \sigma_o^2}}, \tag{2}$$

where $\overline{S_i}$ and $\overline{S_o}$ are the mean signals inside and outside of the target, respectively, and σ_i and σ_o are signal standard deviations of these inside and outside regions, respectively. The ROI was 2 mm (axial) x 12 mm (lateral) and was assigned based on the US B-mode image. The noise (i.e., outside) kernel was of equal size and 1.5 mm above each wire target. This ROI remained fixed for all trials within each study.

2.3. Spectral-fidelity phantom

A tissue-mimicking phantom with an AuNS inclusion was fabricated to assess the effect of depth-dependent scattering on
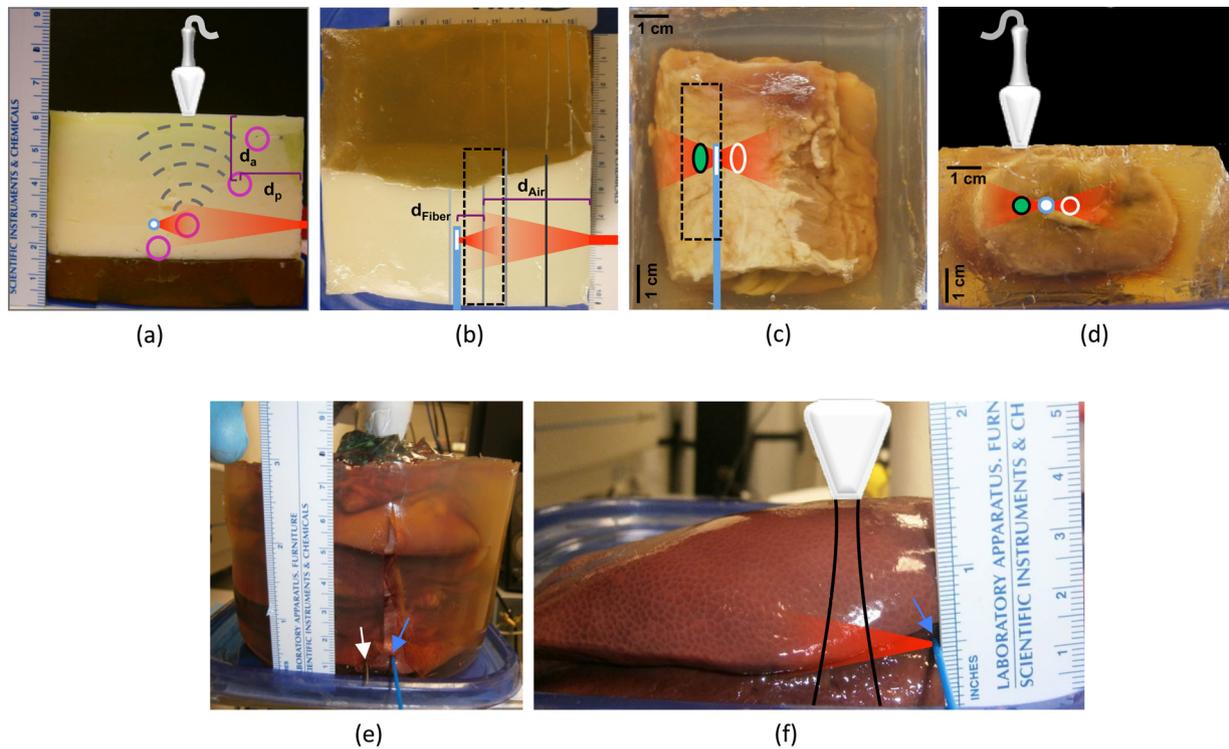
Fig. 3. (a) Side-view of tissue-mimicking phantom with wire inclusions and short-axis outline of transducer provided overhead; purple circles represent location of wires, while blue-white circle denotes location of interstitial fiber; dashed gray lines depict propagation of acoustic waves; external and interstitial irradiation volumes are denoted in red; d_p is distance traveled by photons for external irradiation, while d_a is distance traveled by acoustic wave for both irradiation types. (b) Top-view of phantom; transducer footprint is depicted by black dashed line; blue line represents side-fire imaging fiber location. (c) Top-view of prostate sample; green ellipse represents area of AuNS injection, while white ellipse denotes control region. (d) Side-view of prostate sample. (e) Stack of liver sections cast in pure gelatin for deep interstitial laser delivery; irradiation fiber (blue arrow) and wire imaging target (white arrow) are visible at bottom of image. (f) Liver sample for PA spectroscopy by interstitial laser irradiation; black lines indicate approximate US imaging volume.

multi-wavelength imaging. The AuNS target was multi-spectrally imaged (720, 740, 745, 750, 755, 760, 765, 770, 775, 780, 800, 825, 850, & 900 nm) with both external irradiation (1.7 cm depth from the incident surface and 35-40 mJ with a 0.8 cm² spot size) and interstitial irradiation (6-8 mJ per pulse). All nanoparticle experiments used AuroShell® gold nanoshells (Nanospectra Biosciences, Inc., Houston, TX) that had an optical absorption peak at 760 nm (Fig. 6.c). Absorption profiles were obtained on the AuNS particles using a Synergy™ HT multi-mode microplate reader (BioTek Instruments, Inc., Winooski, VT). For statistical analysis, a 4 mm (axial) x 15 mm (lateral) kernel was utilized.

2.4. Prostate tissue phantom

To demonstrate feasibility of imaging with interstitial irradiation in tissue, the next study in this investigation involved imaging nanoparticle inclusions in ex-vivo bovine prostate tissue (Animal Technologies Inc., Tyler, TX), where the nanoparticle clusters modeled clinical regions of interest such as ablation targets. The prostate tissue was trimmed of all loose fat and abnormalities and then cast in a pure gelatin phantom (8% gelatin; 92% DI H_2O). One site at a depth of approximately 15 mm from the proximal prostate surface was chosen for injection with AuNS particles. In order to prevent migration within the prostate tissue, the particles were suspended in 8% gelatin (1:1 volume ratio) before injection. After injecting the prostate tissue with the particles, the phantom solidified at 4°C for 2 hours. The resulting phantom is shown in Fig. 3.c-d. An 18-gauge needle was used to create a path in the tissue for introduction of the optical fiber approximately 5 mm medial to the inclusions and at equal depth. Images were generated in the region containing nanoparticles as well as in an adjacent control region (i.e., no particles). The targets were

imaged multi-spectrally (same wavelengths used in 2.3) using interstitial irradiation with pulse energies ranging from 6-8 mJ. Data analysis was achieved with a 4 mm (axial) x 6 mm (lateral) kernel about each ROI.

2.5. Liver tissue phantom

2.5.1. Wire imaging

The next study focused on imaging a titanium wire in ex-vivo liver tissue to assess imaging depth in highly absorbing tissue. Ex-vivo porcine liver samples (Animal Technologies Inc., Tyler, TX) were stacked 7.5 cm high and encased in gelatin to prevent movement (Fig. 3.e). A wire target was inserted into the tissue at 7 cm depth from the transducer face; note that the transducer long axis was orientated slightly oblique to the wire. An interstitial irradiation source was then inserted at an equal depth to the wire, 5 mm away laterally, and used to produce a PA signal from the wire. All images were generated using 800 nm irradiation with 8 mJ of energy per pulse.

2.5.2. Deoxyhemoglobin imaging

To demonstrate the multi-wavelength imaging capabilities of interstitial PA imaging and to assess spectral fidelity of an endogenous absorber, ex-vivo liver tissue was multi-spectrally imaged (720, 740, 745, 750, 755, 760, 765, 770, 775, 800, 825, & 850 nm) using only interstitial irradiation (6-8 mJ of energy at the fiber tip) at a depth of 1.6 cm from the transducer (Fig. 3.f). Image analysis kernels (4 mm axial x 4 mm lateral) were centered on points 5.8 mm, 8.1 mm, and 10.4 mm lateral from the distal fiber tip and analyzed to assess the degree of spectral shift (Fig. 7b). PA spectra were compared to the known deoxyhemoglobin absorption spectrum.

2.6. Conical-tip fiber

In an effort to demonstrate the potential of irradiating larger portions of tissue with an interstitial source, the next study imaged wire targets using a clinically-approved optical fiber with a conical termination that provides 360° irradiation about the distal tip (Fig. 2.e and Fig. 8.b). Two wire targets were embedded in gelatin at equal depth, and the optical fiber was inserted between the two, equidistant from each wire. The wires were imaged with the conical-tip fiber (2.5 mJ at 760 nm) at 3 different orientations (i.e., 0°, 90°, 180°) and compared to images generated with a custom-built, side-fire fiber (7 mJ at 760 nm), which only illuminated a sector of the surrounding volume (Fig. 8.a). Note that energy irradiating from the conical-tip fiber was only measured in one direction with the energy meter previously described. For data analysis purposes, a 2 mm (axial) x 2 mm (lateral) kernel was used.

2.7. Fiber-tip artifact

In all trials, the space immediately surrounding the fiber tip was obscured by a PA-signal artifact of unknown origin (white arrows in Fig. 8). In order to attempt to better understand and assess the source of this artifact (i.e., phantom-dependent or fiber-dependent), fiber tips of different varieties were imaged in pure gelatin as well as an absorbing/scattering tissue-mimicking phantom free of all targets. The tissue-mimicking phantom was created using the recipe previously provided with the addition of 0.01% black ink (Drom-gooles Fine Writing Instruments, Houston, TX) to provide an optical density of 1. Beveled and capped fibers, unbeveled and capped fibers, and unbeveled and uncapped fibers were imaged at the fiber tip in both phantom types with contrast values recorded for each. Imaging was performed with 8 mJ of energy at 800 nm, while a 4 mm (axial) x 6 mm (lateral) kernel was used for data analysis.

3. Results

3.1. Tissue-mimicking depth phantom

Results from the tissue-mimicking depth phantom study demonstrate that interstitial irradiation, using significantly less energy, can provide better image quality than external irradiation at photon propagation distances of 13 mm or greater. As seen in Fig. 4, when the dynamic range is kept constant throughout each trial, PA signal from the wire target can be clearly seen at greater depths using interstitial irradiation (i.e., 37, 47 mm), while it is not visible with external irradiation for the same depth range. Some artifacts are present in the images due to reverberation in the wire target and a near-field artifact resulting from transducer crosstalk. Additionally, as shown in Fig. 5.b, the SNR resulting from external irradiation decreases from 41.8 at 7 mm depth to 0.95 at 47 mm in depth, while the SNR resulting from interstitial irradiation ranges from 53.1 to 25.3 over the same depth span. In a similar fashion (Fig. 5.c), the CNR resulting from external irradiation decreases from 0.99 to 0.07 over the course of increased imaging depth, while the CNR resulting from interstitial irradiation only decreases from 1.12 to 1.07.
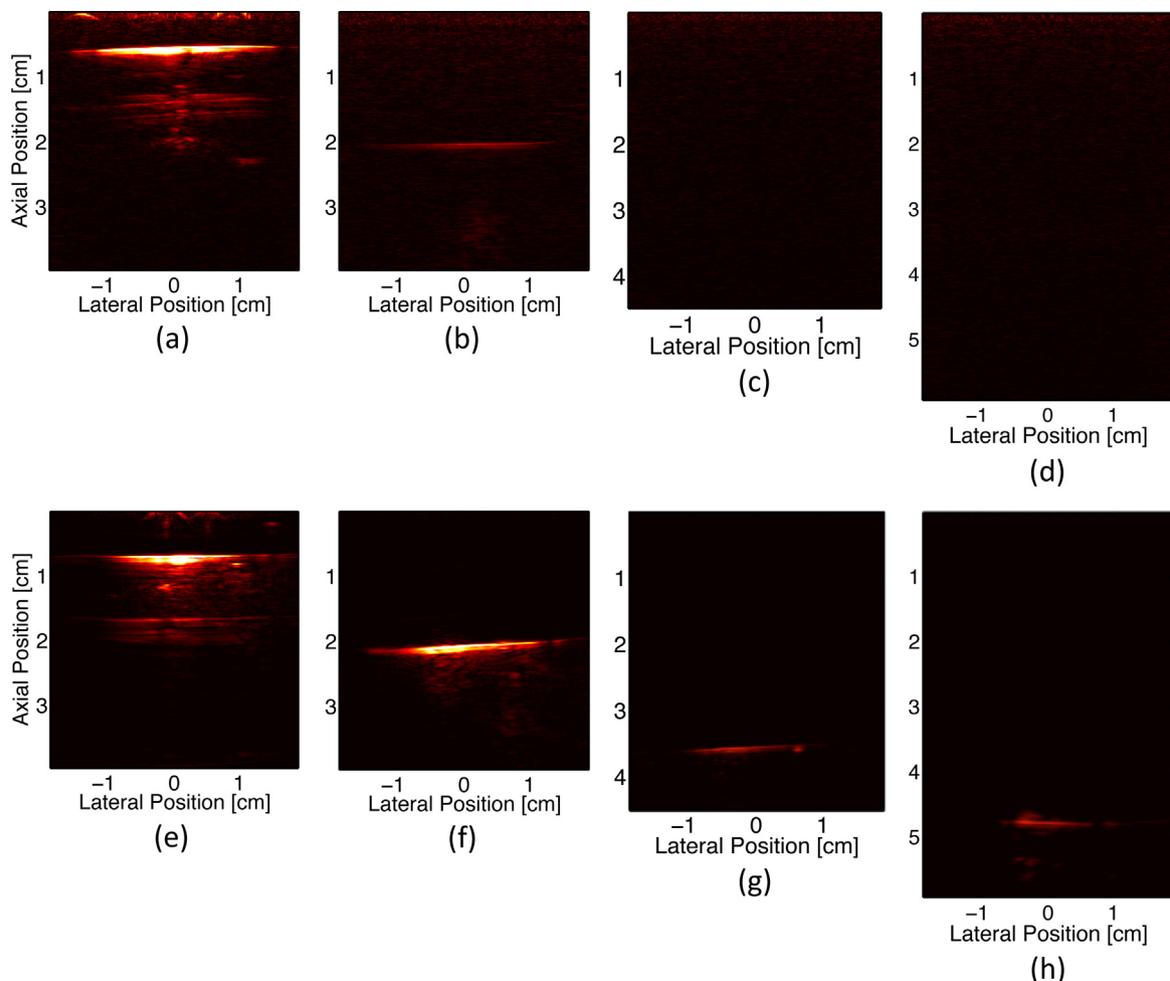

Fig. 4. PA images of wire at different depths (7, 20, 37, & 47 mm depths) in a tissue-mimicking phantom. (a)–(d) PA imaging driven by external irradiation; (e)–(h) PA imaging driven by interstitial irradiation. Note dynamic range is kept constant for all images of same irradiation type.
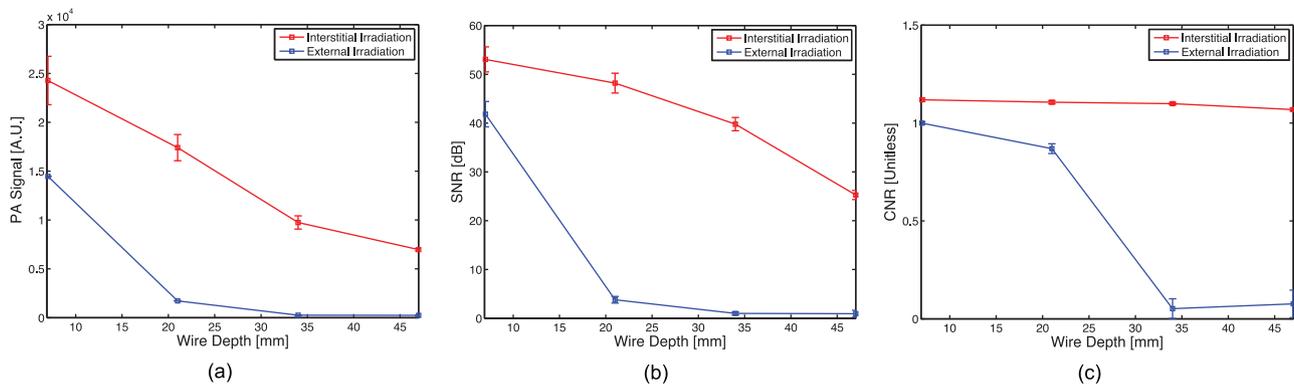
Fig. 5. (a) PA signal, (b) SNR, and (b) CNR plot (N = 10) comparison of PA imaging of wires at increasing depth driven by interstitial (red) or external (blue) irradiation.

3.2. Spectral-fidelity phantom

Results from the spectral fidelity study show that interstitial imaging provides more accurate spectral information than traditional irradiation methods in a tissue-mimicking phantom. The nanoparticles imaged had broadband absorption in the low-NIR range, with an absorption peak at 760 nm. As can be seen in Fig. 6.a, interstitial irradiation provided an absorption spectrum which peaked at 760 nm and generally decreased monotonically away from this peak. Conversely, traditional irradiation methods produced an absorption spectrum which peaked at 800 nm, demonstrating a redshift inherent to traveling through scattering tissue.

3.3. Prostate tissue phantom

Results from the prostate tissue phantom study demonstrate that it is possible to spectroscopically identify specific photoabsorbers using interstitial irradiation in ex-vivo tissue. As shown in Fig. 6.b, the signal from the region containing nanoparticles can clearly be discerned when compared to the control region. The signal from the injection site closely matches the absorption spectrum of the injected nanoparticles, while the signal from the control (i.e., non-injected) site strongly resembles the spectrum of deoxyhemoglobin (Fig. 6.c).

3.4. Liver tissue phantom

3.4.1. Wire imaging

Results from the ex-vivo liver phantom show that PA signals generated 7 cm from the transducer face in a highly absorbing medium using only 8 mJ of energy in the low-NIR range can be readily imaged. Fig. 7.a shows the image of the embedded titanium target generated by interstitial irradiation.

3.4.2. Deoxyhemoglobin imaging

Results from the ex-vivo liver imaging study also indicate that endogenous absorbers can be spectroscopically isolated at depth. Approximately two centimeters deep from the transducer face, the spectroscopic PA signal (Fig. 7.c) obtained from the three regions of excised liver tissue correlated very strongly with that of deoxyhemoglobin (Fig. 7.d). The imaged signals all have the characteristic deoxyhemoglobin "hump" at approximately 758 nm. However, as distance from the fiber tip increases, spectral fidelity decreases as a red-shift in the spectra occurs. Interstitial irradiation at 5 mm from the fiber tip causes minimal shift in the signal with approximately 1.3 nm of redshift for every millimeter increase in distance from the fiber tip observed.

3.5. Conical-tip fiber

The results from the conical-tip fiber studies show that 360° irradiation of target tissue, which is not possible with a simple beveled fiber, is achievable through the use of a conical tip. The signal generated by each wire was approximately equal when irradiated with the conical tip, while at most only one wire generated signal when irradiated by the beveled tip, as seen in Fig. 8. Contrast values for the right and left wires using the side-fire fibers were 7.19 (0°) and 9.37 (180°), respectively, when directly irradiated and 2.35 or less when not directly irradiated (e.g., right wire in Fig. 8.e). For the conical-tip fiber, contrast values ranged from 2.07 to 3.47 for all rotation orientations and wires. This fiber removes the directional component introduced by the beveled
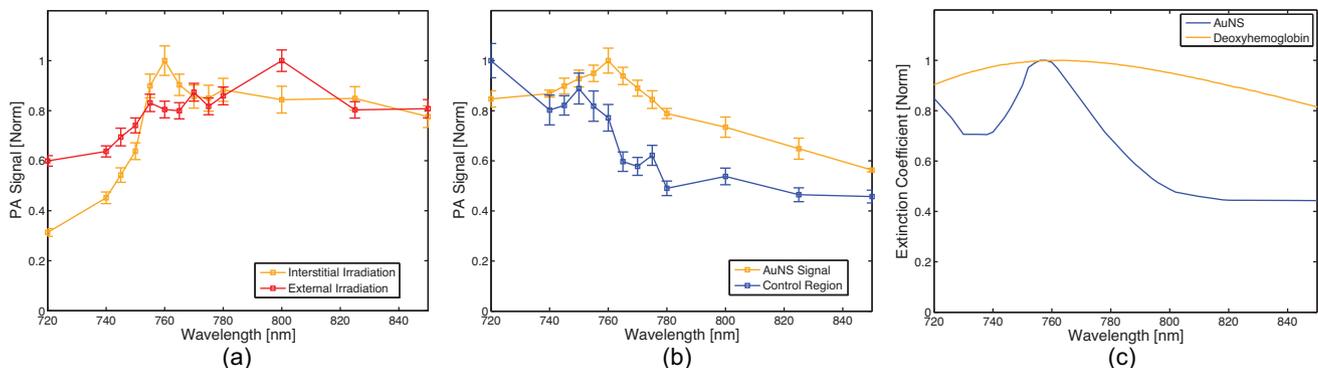

Fig. 6. (a) PA signal spectrum (N = 30) generated by AuNSs in tissue-mimicking phantom using external irradiation (red) with a 17-mm photon propagation distance or interstitial irradiation (gold) with a 5-mm photon propagation distance; (b) PA signal spectrum (N = 30) generated by AuNSs (gold) or deoxyhemoglobin (blue) in ex-vivo prostate tissue using interstitial irradiation; (c) Optical absorption spectrum of AuNSs (gold) and deoxyhemoglobin (blue).
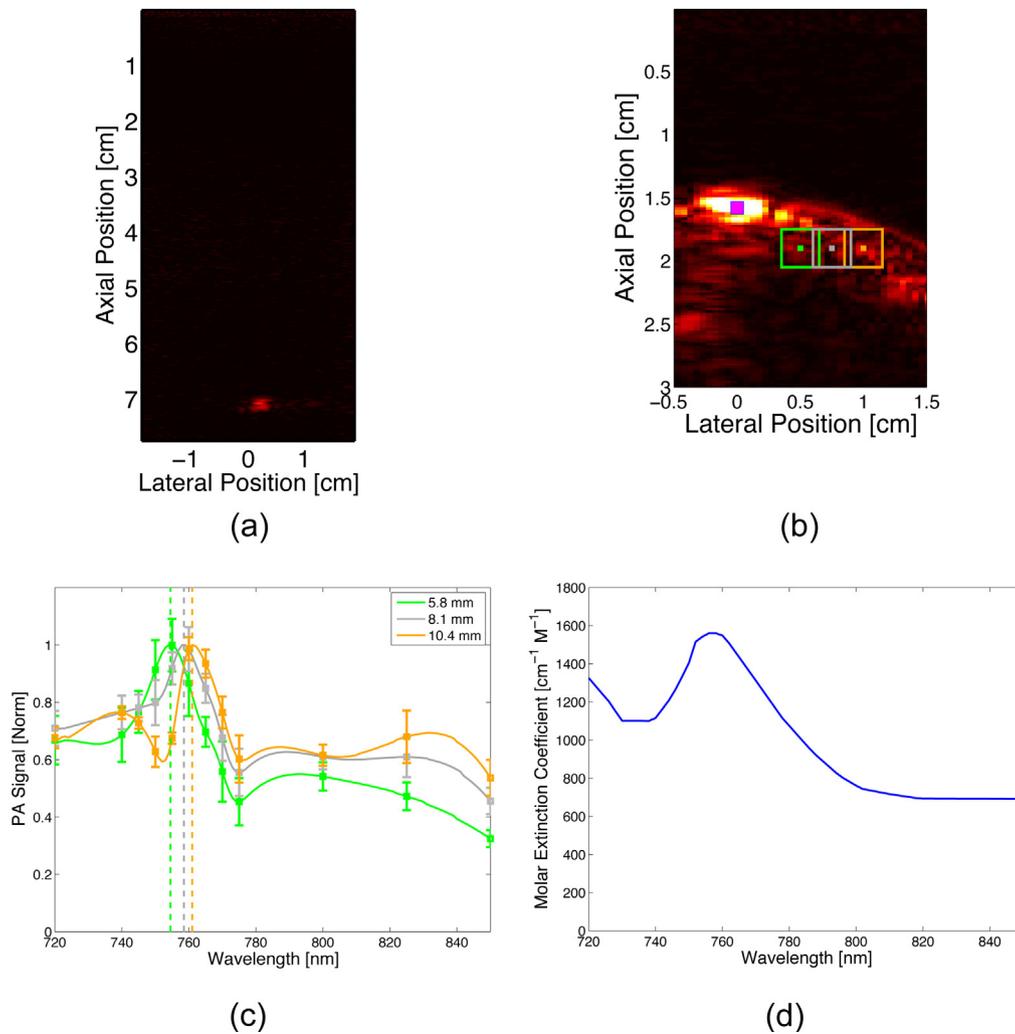
Fig. 7. (a) PA image of wire embedded in ex-vivo liver at 7 cm. (b) PA image of hemoglobin in ex-vivo liver at approximately 2 cm. Magenta spot represents center of fiber, while green, grey, and gold boxes represent kernels for 5.8-mm, 8.1-mm, and 10.4-mm analysis, respectively; dot in center of kernel denotes measurement point (i.e., where distance from the source was measured). (c) Multi-wavelength acquisition (N = 30) of deoxyhemoglobin target at distances of 5.8 mm (green), 8.1 mm (grey), and 10.4 mm (gold) from the inserted fiber tip. (d) Optical absorption spectrum of deoxyhemoglobin [20].

fiber tip; although, due to the lower output fluence inherent to this fiber, the overall contrast values are lower. Additionally, this study showed that optical fibers used in the clinic can be repurposed for use in fiber-driven PA imaging.

3.6. Fiber-tip artifact

This study demonstrated that all fiber types in the imaging environments tested generate a PA-signal artifact at their distal tip when imaging. For beveled, straight-capped, and straight-uncapped fibers in gelatin, the contrast values were 27.1 dB, 29.4 dB, and 31.6 dB, respectively, while in an absorbing/scattering tissue-mimicking phantom, the contrast values were 34.7, 40.6, and 36.7, dB, respectively. There was an increase in PA signal for all fiber types when imaging in the tissue-mimicking phantom compared to pure gelatin.

4. Discussion

We have demonstrated that it is feasible to generate a PA image using interstitial irradiation with an external US receive-array. In this study, interstitial irradiation has revealed improved interrogation depth compared to conventional external irradiation. Using an interstitially placed optical fiber, PA images were readily achieved at depths of 7 cm in tissue using only 8 mJ (40 $\frac{mJ}{cm^2}$ at 5 mm), while multi-wavelength imaging was demonstrated 2 cm into tissue. The interstitial irradiation technique investigated maintained better image quality (i.e., SNR, CNR) and spectral fidelity at all depths tested when compared to conventional external irradiation.

Although both beveled-tip and conical-tip fibers were used in this study, potential clinical applications would likely implement an interstitial irradiation fiber with a conical tip in order to achieve a larger irradiation volume (i.e., prostate biopsy). Further modifications to the irradiation fiber may be required for actual clinical application. For instance, a diffuser could be used during 360° irradiation with the conical tip fiber, permitting more of the tissue sample to be imaged at a time and providing a more uniform light distribution [21].

While the fluence levels generated at 5 mm during interstitial irradiation do slightly exceed the acknowledged ANSI limit for skin exposure at some wavelengths (e.g., 30 $\frac{mJ}{cm^2}$ at 720 nm versus the 22 $\frac{mJ}{cm^2}$ limit for skin), this fluence would not applied to skin but rather would be inserted directly into soft tissue, which tends to have lower absorption and scattering than skin over the wavelength range used [22,23]. It is also important to note that no tissue damage was noted in any trials using interstitial irradiation, nor
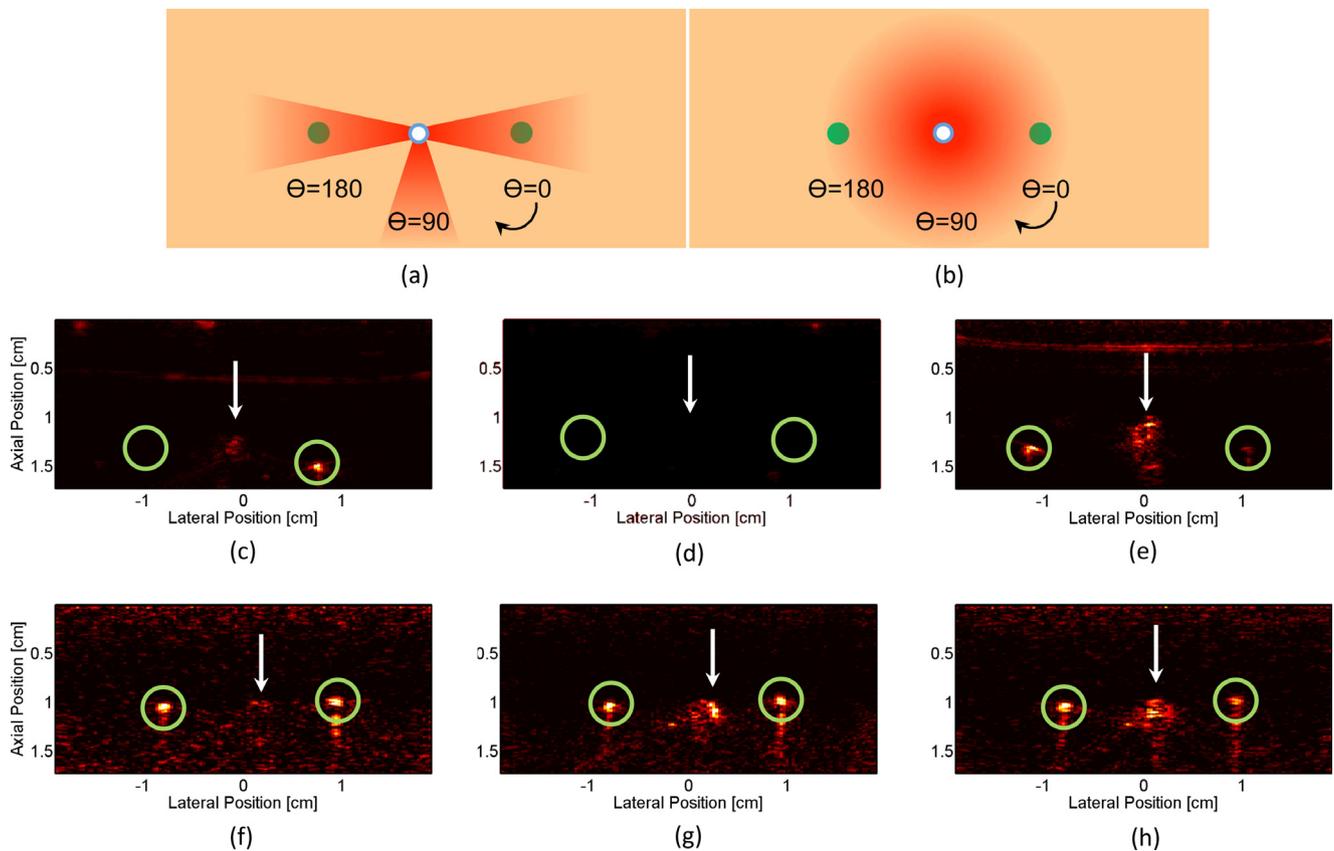
Fig. 8. Side-fire and conical-tip fiber comparison. (a) Illustration of side-fire fiber rotation and irradiation pattern; green circles represent location of wires, while blue-white circle indicates position of fiber tip. (b) Illustration of conical-tip fiber rotation and irradiation pattern. (c) - (h) PA images of two wires embedded in gelatin; white arrows denote PA-signal artifact at fiber location, and green circles outline PA signal generated from wires. PA images generated from side-fire irradiation at (c) 0°, (d) 90°, and (e)180° rotation. PA images generated from conical-tip irradiation at (f) 0°, (g) 90°, and (h) 180° rotation.

were any spectral changes noticed in the tissue samples due to ablative processes. Although fluence levels at 5 mm from the distal fiber tip are likely to be safe for clinical use, one concern that must be addressed before clinical adoption is that of high-fluence regions immediately surrounding the fiber tip before the light begins to diffuse. While more research is needed to determine appropriate fluence levels for interstitial irradiation, it is likely that soft tissue can withstand greater fluence levels than skin in the low-NIR range. Should concerns over fluences proximal to the tip be an issue, it could be possible to either increase the diameter of the fiber end-cap and/or add a diffuser (e.g., inflatable balloon tip with a scattering fluid) around the fiber tip to control local fluence levels at the source and thereby protect nearby tissue.

There are instances in the presented results where the PA signal spectra slightly differ from known absorption spectra. One cause for this could be imprecision in wavelength calibration when using the aforementioned spectrometer. Additionally, at lower wavelengths, increased scattering and absorption can cause a decrease in signal beyond what is corrected for by energy normalization, leading to a slight skewing of the data at these wavelengths.

During testing, an artifact appeared in some PA images that was caused from the generation of a PA signal by the irradiating tip of the interstitial fiber. This artifact appeared independent of the imaging medium, occurring in both pure gelatin and tissue-mimicking phantoms. One potential explanation for this artifact is that proximal chromophores adjacent to the fiber tip absorb energy where fluence would be highest (i.e., before tissue scattering occurs). In the case of gelatin phantoms, the water used in the phantom could provide the source of absorption. Despite the low optical absorption of water in the low-NIR range,

the relatively high fluence at the fiber tip could be enough to induce an appreciable PA effect [20]. One further possibility is that mismatched refractive indices at the insertion site (i.e., water-tissue interface immediately surrounding the fiber tip) causes light to backscatter, which could manifest as a fluence gain in the tissue immediately surrounding the fiber tip. Continued classification of the tip artifact will allow for improved imaging using interstitial fibers.

To implement interstitial irradiation, an optical fiber must be introduced percutaneously in order for light to reach the target tissue. Current minimally invasive, standard-of-care techniques common in IR, such as thermal ablations and image-guided biopsies, could reasonably accommodate the optical fiber through placement alongside or following the extraction of interstitial instruments. During photothermal ablation, a fiber delivering the output of a CW laser is already in place within the target tissue [24,25]. To incorporate PA guidance into photothermal therapy, a single optical fiber would remain in place, while the laser source could be switched between the CW source for treatment and the pulsed source required for PA imaging. Radiofrequency (RF) ablation techniques could also be adapted to include an interstitial optical fiber to provide PA imaging to monitor liver and cardiac ablation procedures [26].

PA imaging techniques are also capable of monitoring tissue state during ablative procedures by utilizing thermography and spectroscopy to assess oxygen saturation, tissue denaturation, and temperature [27–29]. In both RF and photothermal ablation techniques, real-time PA-based thermography could be used to monitor the temperature of critical structures adjacent to the ablation target, while assessment of oxygen saturation or tissue

denaturation could be used as a treatment endpoint, thereby providing precise treatment margins [30,31]. However, should clinical fluence value recommendations fall below the values presented, further investigation of the effect of SNR on spectral unmixing in in-vivo animal models will be necessary.

Needle biopsies also provide a practical pathway for interstitial irradiation. During biopsies, real-time PA spectroscopy could be applied for identification of normoxic and hypoxic tissue. Hypoxic or necrotic tissue is characteristic of the core of a fast-growing, possibly aggressive tumor, therefore the clinician could adapt the sampling locations based on the tissue's oxygen state, which could later also be used to inform radiation treatment planning [32]. A typical biopsy needle has a diameter of at least 1.27 mm (18-gauge), which could easily accommodate the 1000-μm optical fibers implemented in this preliminary investigation.

By utilizing B-mode images from the existing US array in concert with interstitial PA imaging, the interstitial irradiation source would be co-registered with the imaging plane, while the B-mode images would provide anatomical visualization and context of surrounding tissue structures during a clinical procedure [2]. Photoacoustic imaging driven by an interstitial irradiation source, especially if combined with the proven anatomical visualization capabilities of B-mode imaging, shows great promise for IR applications due to its potential to guide and monitor minimally invasive procedures and its compatibility with existing clinical equipment and workflow.

5. Conclusion

This work demonstrated the feasibility of using an interstitial source to provide sufficient local fluence in generating reliable PA images that are acquired with an external US array. Multi-wavelength PA imaging was demonstrated on nanoparticle targets in ex-vivo tissue and in tissue-mimicking phantoms. Similar imaging techniques could be used in clinical procedures to provide real-time feedback during PA image-guided biopsies or thermal therapy. As demonstrated by the results of this feasibility study, the clinical role of PA imaging in the future can be further expanded by implementing local, interstitial irradiation for characterizing deeper tissues using conventional clinical US systems.

Conflict of Interest Statement

The authors declare that there are no conflicts of interest.

Acknowledgements

References

[1] Cleary K, Peters TM. Image-guided interventions: technology review and clinical applications. Annual Review of Biomedical Engineering 2010;12: 119–42.

[2] Bouchard R, Sahin O, Emelianov S. Ultrasound-guided photoacoustic imaging: current state and future development, Ultrasonics, Ferroelectrics and Frequency Control. IEEE Transactions on 2014;61(3):450–66.

[3] Karabutov AA, Podymova NB, Letokhov VS. Time-resolved laser optoacoustic tomography of inhomogeneous media 1996.

[4] Laser Institute of America, ANSI Z136.1: American National Standard for Safe Use of Lasers, Tech. rep., American National Standards Institute, Laser Institute of America, Orlando, FL (2007).

[5] Homan K, Kim S, Chen Y-S, Wang B, Mallidi S, Emelianov S. Prospects of molecular photoacoustic imaging at 1064 nm wavelength. Optics letters 2010;35(15):2663–5.

[6] Simpson CR, Kohl M, Essenpreis M, Cope M. Near-infrared optical properties of ex vivo human skin and subcutaneous tissues measured using the Monte Carlo inversion technique. Physics in Medicine and Biology 1998;43:2465–78.

[7] Su JL, Bouchard RR, Karpiouk AB, Hazle JD, Emelianov SY. Photoacoustic imaging of prostate brachytherapy seeds. Biomedical Optics Express 2011;2(8):2243–54.

[8] Mitcham T, Homan K, Frey W, Chen Y-S, Emelianov S, Hazle J, Bouchard R. Modulation of photoacoustic signal generation from metallic surfaces. Journal of biomedical optics 2013;18(5). 056008–056008.

[9] Yuan Y, Yang S, Xing D. Preclinical photoacoustic imaging endoscope based on acousto-optic coaxial system using ring transducer array. Optics Letters 2010;35:2266–8.

[10] Sheaff C, Lau N, Patel H, Huang SW, Ashkenazi S. Photoacoustic imaging endoscope. In: Annual International Conference of the IEEE Engineering in Medicine and Biology Society 2009. 2009. p. 1983–6.

[11] Yang J-M, Favazza C, Chen R, Yao J, Cai X, Maslov K, Zhou Q, Shung KK, Wang LV. Simultaneous functional photoacoustic and ultrasonic endoscopy of internal organs in vivo. Nature Medicine 2012;18:1297–302.

[12] Karpiouk AB, Wang B, Emelianov SY. Development of a catheter for combined intravascular ultrasound and photoacoustic imaging. Review of Scientific Instruments 2010;81(1):014901.

[13] Jansen K, Van Der Steen AF, Springeling G, Van Beusekom HM, Oosterhuis JW, Van Soest G. Intravascular photoacoustic imaging of human coronary athero-sclerosis. In: SPIE BiOS, International Society for Optics and Photonics; 2011. 789904–789904.

[14] Mitcham T, Marques T, Chatterjee D, Krishnan S, Pugh T, Bouchard R. Trans-rectal photoacoustic-ultrasonic imaging enhancement through interstitial irradiation and targeted nanoparticles. In: Proceedings of the 2013 IEEE Ultrasonics Symposium; 2013.

[15] Yamamoto S, Nishida T, Kato M, Inoue T, Hayashi Y, Kondo J, Akasaka T, Yamada T, Shinzaki S, Iijima H, Tsujii M, Takehara T. Evaluation of endoscopic ultrasound image quality is necessary in endosonographic assessment of early gastric cancer invasion depth. Gastroenterology Research and Practice 2012.

[16] Gazelle GS, Haaga JR, Rowland DY. Effect of needle gauge, level of antic-oagulation, and target organ on bleeding associated with aspiration biopsy. work in progress. Radiology 1992;183(2):509–13.

[17] Cook JR, Bouchard RR, Emelianov SY. Tissue-mimicking phantoms for photo-acoustic and ultrasonic imaging. Biomedical optics express 2011;2(11):3193–206.

[18] Dahl JJ, Pinton GF, Palmeri ML, Agrawal V, Nightingale KR, Trahey GE. A parallel tracking method for acoustic radiation force impulse imaging, Ultrasonics, Ferroelectrics and Frequency Control. IEEE Transactions on 2007;54(2):301–12.

[19] Bouchard RR, Dahl JJ, Hsu SJ, Palmeri ML, Trahey GE. Image quality, tissue heating, and frame rate trade-offs in acoustic radiation force impulse imaging, Ultrasonics, Ferroelectrics and Frequency Control. IEEE Transactions on 2009;56(1):63–76.

[20] S. Prahl, Optical properties spectra, accessed: 2014-07-01 (2001). URL http://omlc.org/spectra/.

[21] Lediju Bell MA, Kuo N, Song DY, Boctor EM. Short-lag spatial coherence beamforming of photoacoustic images for enhanced visualization of prostate brachytherapy seeds. Biomedical optics express 2013;4(10):1964–77.

[22] Anderson RR, Parrish JA. The optics of human skin. Journal of Investigative Dermatology 1981;77(1):13–9.

[23] Dawson J, Barker D, Ellis D, Cotterill J, Grassam E, Fisher G, Feather J. A theoretical and experimental study of light absorption and scattering by in vivo skin. Physics in medicine and biology 1980;25(4):695.

[24] Lindner U, Weersink RA, Haider MA, Gertner MR, Davidson SRH, Atri M, Wilson BC, Fenster A, Trachtenberg J. Image guided photothermal focal therapy for localized prostate cancer: phase i trial. The Journal of urology 2009;182(4): 1371–7.

[25] Nanospectra Biosciences Inc., Pilot study of AuroLase therapy in refractory and/or recurrent tumors of the head and neck, Tech. Rep. April 2008, Baylor College of Medicine, Houston, TX (2014).

[26] Garcea G, Lloyd T, Aylott C, Maddern G, Berry DP. The emergent role of focal liver ablation techniques in the treatment of primary and secondary liver tumours. European Journal of Cancer 2003;39(15):2150–64.

[27] Zhang HF, Maslov K, Sivaramakrishnan M, Stoica G, Wang LV. Imaging of hemoglobin oxygen saturation variations in single vessels in vivo using photoacoustic microscopy. Applied Physics Letters 2007;90(5):053901.

[28] Welch AJ, van Gemert MJ. Optical-Thermal Response of Laser-Irradiated Tissue. Springer; 2011.

[29] Shah J, Park S, Aglyamov S, Larson T, Ma L, Sokolov K, Johnston K, Milner T, Emelianov SY. Photoacoustic imaging and temperature measurement for photo-thermal cancer therapy. Journal of Biomedical Optics 2008;13(3):034024.

[30] Lee HJ, Liu Y, Zhao J, Zhou M, Bouchard RR, Mitcham T, Wallace M, Stafford RJ, Li C, Gupta S, Melancon MP. In vitro and in vivo mapping of drug release after laser ablation thermal therapy with doxorubicin-loaded hollow gold nano-shells using fluorescence and photoacoustic imaging. Journal of Controlled Release Society 2013;172(1):152–8.

[31] Dana N, Di Biase L, Natale A, Emelianov S, Bouchard R. In vitro photoacoustic visualization of myocardial ablation lesions. Heart Rhythm 2014;11(1):150–7.

[32] Mallidi S, Luke GP, Emelianov S. Photoacoustic imaging in cancer detection, diagnosis, and treatment guidance. Trends in Biotechnology 2011;29(5):213–21.

Trevor Mitcham received his B.S. degree is Bioengineering at Rice University in 2012. He is currently a graduate student in Medical Physics at the University of Texas at Houston and the University of Texas MD Anderson Cancer Center Graduate School of Biomedical Sciences in Houston, Texas. His research interests include photoacoustic imaging for diagnostics and therapy guidance.

Katherine Dextraze is currently pursuing her Ph.D. in Medical Physics at the Graduate School of Biomedical Sciences in Houston, Texas. Her research interests include photoacoustic imaging and image guidance for minimally invasive procedures. She received her B.S. degree in 2011 in Nuclear and Radiological Engineering at the Georgia Institute of Technology in Atlanta, GA. She was granted a specialized M.S. degree in 2013 in Medical Physics from the University of Texas at Houston and the University of Texas MD Anderson Cancer Center Graduate School of Biomedical Sciences.

Houra Taghavi received her B.S. degree in Electrical Engineering from Azad University, Iran and M.S. degree in Biomedical Engineering at Texas A&M University in 2013. She is currently a researcher at the University of Texas MD Anderson Cancer Center. Her research interests include integrated ultrasound and photoacoustic imaging and nanoparticle contrast agents in photoacoustic imaging.

Marites Melancon is an Assistant Professor in the Department of Interventional Radiology at The University of Texas MD Anderson Cancer Center. She earned her B.S. degree in Chemistry from the University of San Carlos (Cebu, Philippines) and her M.S. degree in Chemistry at Ateneo de Manila University (Manila, Philippines). She received her Ph.D. degree in Biomedical Science at The University of Texas Health Science Center at Houston in 2007. Research in the Melancon laboratory is primarily focused on the development of therapeutic and diagnostic agents for image-guided interventions.

Richard Bouchard received his B.S. degree in Biomedical and Electrical engineering and Cultural Anthropology from Duke University in 2004 and received his Ph.D. degree in Biomedical Engineering from Duke University in 2010. He completed a postdoctoral fellowship in the Ultrasound Imaging and Therapeutics Research Laboratory at the University of Texas at Austin in 2012. Dr. Bouchard is currently an Assistant Professor in the Department of Imaging Physics at the University of Texas MD Anderson Cancer Center. His research interests include preclinical and clinical photoacoustic-ultrasonic imaging and ultrasound-based elasticity imaging.